

# cuRAMSES: Scalable Domain Decomposition and CUDA-enabled AMR for Cosmological Simulations

Juhan Kim<sup>1\*</sup>

<sup>1</sup>Center for Advanced Computation, Korea Institute for Advanced Study, 85 Hoegiro, Dongdaemun-gu, Seoul 02455, Republic of Korea

Accepted XXX. Received YYY; in original form ZZZ

## ABSTRACT

We present cuRAMSES, a suite of algorithmic and implementation improvements to the RAMSES adaptive mesh refinement (AMR) cosmological simulation code that address the principal bottlenecks encountered in large-scale simulations: communication overhead, memory consumption, and solver efficiency. The central innovation is a recursive  $k$ -section domain decomposition that replaces the traditional Hilbert curve ordering with a hierarchical spatial partitioning, dramatically reducing the number of MPI messages per ghost-zone exchange and eliminating all MPI\_ALLTOALL calls. A Morton key hash table for octree neighbour lookup removes one of the largest per-rank arrays in the original code, while on-demand allocation strategies for auxiliary arrays further reduce the memory footprint. A hybrid CPU/GPU dispatch model allows OMP threads to dynamically offload compute-intensive routines — including the Godunov solver, gravity force computation, and radiative cooling — to GPU streams at runtime, with automatic fallback to CPU execution when streams are unavailable. We also implement variable- $N_{\text{cpu}}$  restart for both HDF5 and native binary output formats, removing the constraint that output files must be read with the same number of MPI ranks as were used to write them. All modifications preserve physical consistency, as verified by conservation-law diagnostics across extensive test suites.

**Key words:** methods: numerical – cosmology: simulations – hydrodynamics – software: development

## 1 INTRODUCTION

Cosmological hydrodynamic simulations play a central role in modern astrophysics, connecting the predictions of the  $\Lambda$ CDM paradigm to the observable properties of galaxies, the intergalactic medium, and the large-scale structure of the Universe. Over the past decade, a series of landmark galaxy formation simulations have advanced our understanding of cosmic structure: the Illustris and IllustrisTNG projects (Vogelsberger et al. 2014; Pillepich et al. 2018; Nelson et al. 2019) using the moving-mesh code AREPO (Springel 2010), the EAGLE simulation (Schaye et al. 2015) with the smoothed-particle hydrodynamics code GADGET (Springel 2005), the Horizon-AGN simulation (Dubois et al. 2014) and its high-resolution successor NewHorizon (Dubois et al. 2021) using the adaptive mesh refinement (AMR) code RAMSES (Teyssier 2002), and the FIRE project (Hopkins et al. 2018) with the meshless finite-mass code GIZMO (Hopkins 2015).

Among the numerical approaches employed by these simulations, AMR codes such as RAMSES and Enzo (Bryan et al. 2014) provide a particularly attractive framework: the computational mesh is refined only where the physics demands it, concentrating resources on collapsing haloes and star-forming regions while keeping the cost of smooth, low-density regions manageable.

A key design choice in parallel AMR codes is the domain decomposition strategy. Space-filling curves (SFCs), particularly the Hilbert (Peano–Hilbert) curve, have been widely adopted for this purpose (Warren & Salmon 1993; Springel 2005). The Hilbert curve maps the three-dimensional computational domain to a one-dimensional index, preserving spatial locality so that cells close in physical space remain close along the curve. This enables a simple and effective partitioning: the one-dimensional index range is divided into  $N_{\text{cpu}}$  contiguous segments, each assigned to an MPI rank. The resulting decomposition naturally produces compact subdomains with relatively small surface-to-volume ratios, minimising the ghost-zone boundary between neighbouring ranks.

However, scaling this approach to the regime of  $10^{10}$ – $10^{11}$  particles and  $10^4$ – $10^5$  MPI ranks reveals fundamental limitations. The one-dimensional nature of the SFC means that *every* rank may, in principle, border *any other* rank, forcing communication patterns that scale poorly with  $N_{\text{cpu}}$ . In the standard RAMSES implementation, ghost-zone exchange, grid and particle migration, and sink particle synchronisation all rely on MPI\_ALLTOALL to communicate counts among all ranks, leading to  $\mathcal{O}(N_{\text{cpu}}^2)$  message complexity and  $\mathcal{O}(N_{\text{cpu}})$  per-rank buffer memory — a severe bottleneck when  $N_{\text{cpu}}$  exceeds  $\sim 10^3$  (Teyssier 2002). Furthermore, the Hilbert ordering distributes load based on cell count alone, which becomes increasingly inadequate for cosmological simulations where the particle distribution is highly clustered: a cell hosting  $10^4$

\* E-mail: kjhan@kias.re.kr

52 particles in a dense halo is far more expensive in memory than 114  
 53 a void cell with zero particles, yet the standard load balancer 115  
 54 treats them equally (Springel 2005). The problem is partic- 116  
 55 ularly acute in cosmological zoom-in simulations (Dubois et 117  
 56 al. 2021), where the high-resolution region occupies a small 118  
 57 fraction of the total volume: the Hilbert curve concentrates 119  
 58 nearly all refinement on a few ranks while the remaining ranks 119  
 59 are left with low-resolution void cells, leading to severe load 119  
 60 imbalance that worsens with increasing zoom factor. 119

61 Beyond the communication and load-balancing chal- 120  
 62 lenges, several other bottlenecks arise. Large per-rank ar- 120  
 63 rays scale linearly with  $N_{\text{gridmax}}$ : the neighbour-pointer ar- 121  
 64 ray `nbor(N_{\text{gridmax}}, 6)` alone consumes  $48 N_{\text{gridmax}}$  bytes 122  
 65 (Teyssier 2002), and the Hilbert key array adds another 123  
 66 16  $N_{\text{gridmax}}$  bytes (when compiled with QUADHILBERT), to- 124  
 67 gether approaching 1 GB per rank for production configu- 125  
 68 rations with  $N_{\text{gridmax}} \sim 5$  M. The multigrid Poisson solver 126  
 69 (Guillet & Teyssier 2011) typically dominates runtime, its 127  
 70 per-iteration cost driven by frequent ghost-zone exchanges 128  
 71 and repeated hash table lookups for neighbour grids. Finally, 129  
 72 RAMSES writes one file per MPI rank, so restarting with a 130  
 73 different rank count is practically infeasible: the AMR tree 131  
 74 structure — parent-child links, neighbour pointers, and per- 132  
 75 rank communication tables — is tightly coupled to the origi- 133  
 76 nal domain decomposition and cannot be reconstructed with- 134  
 77 out re-reading and redistributing every grid from scratch. 135

78 The original RAMSES code relies exclusively on MPI for 136  
 79 parallelism, assigning one MPI rank per processor core. To 137  
 80 exploit the shared-memory bandwidth of modern multi-core 138  
 81 nodes, hybrid MPI+OpenMP implementations have been de- 139  
 82 veloped: the Horizon Run 5 simulation (Lee et al. 2021) em- 140  
 83 ploys OMP-RAMSES, and the NewCluster zoom-in simula- 141  
 84 tion (Han et al. 2026) employs RAMSES-yOMP, both adding 141  
 85 OpenMP threading within each MPI rank for improved intra- 141  
 86 node scalability. However, MPI+OpenMP alone still leaves 142  
 87 the GPU compute capability of modern heterogeneous nodes 142  
 88 untapped. With the emergence of exascale supercomputers 143  
 89 whose floating-point throughput is dominated by GPU ac- 144  
 90 celerators, a three-level MPI+OpenMP+CUDA parallelism 144  
 91 is essential to fully utilise the available hardware. 145

92 In this paper we describe CURAMSES, a comprehensive 146  
 93 set of modifications to RAMSES that addresses each of these 146  
 94 challenges. We introduce a recursive  $k$ -section domain de- 147  
 95 composition (Section 2) that replaces Hilbert ordering with 147  
 96 a hierarchical multi-way spatial partitioning, enabling MPI 147  
 97 exchange with  $\mathcal{O}(\sum_l k_l)$  messages per operation. A Morton 147  
 98 key hash table (Morton 1966) (Section 4) eliminates the `nbor` 148  
 99 array entirely, saving  $\sim 240$  MB per rank, and on-demand al- 149  
 100 location of redundant large arrays (Section 5) yields over 150  
 101 1 GB of additional savings. Algorithmic optimizations to the 151  
 102 multigrid Poisson solver (Section 6) reduce its share of to- 152  
 103 tal runtime from 55 per cent to 39 per cent, while a spatial 153  
 104 hash binning scheme (Section 7) accelerates Type II super- 154  
 105 nova and AGN feedback by orders of magnitude. We also 155  
 106 implement variable- $N_{\text{cpu}}$  restart for both HDF5 and binary 156  
 107 formats (Section 8), along with miscellaneous improvements 157  
 108 described in Section 9. A hybrid CPU/GPU dispatch model 158  
 109 (Section 10) dynamically offloads compute-intensive routines 159  
 110 to GPU streams at runtime. Performance benchmarks are 160  
 111 presented in Section 11, and we conclude in Section 12. 161

112 Throughout this paper, we use the notation of Teyssier 162  
 113 (2002):  $N_{\text{levelmax}}$  is the maximum AMR level,  $N_{\text{gridmax}}$  is the 163

maximum number of grids per rank, `twotondim` =  $2^{N_{\text{dim}}}$  = 8 is the number of cells per oct in three dimensions, and  $N_{\text{cpu}}$  is the total number of MPI ranks.

## 2 RECURSIVE K-SECTION DOMAIN DECOMPOSITION

### 2.1 Motivation

The standard RAMSES domain decomposition assigns cells to MPI ranks by sorting them along a Hilbert space-filling curve and partitioning the resulting one-dimensional index range into  $N_{\text{cpu}}$  contiguous segments. While this preserves spatial locality reasonably well, it has two significant drawbacks for large-scale runs. First, the ghost-zone exchange requires `MPI_ALLTOALL` to communicate emission/reception counts, followed by point-to-point messages to all ranks with non-zero counts; in the worst case, every rank communicates with every other rank, yielding  $\mathcal{O}(N_{\text{cpu}}^2)$  total messages. Second, the Hilbert key computation requires a large per-rank array `hilbert_key(1:ncell)` of 16 bytes per cell (when compiled with QUADHILBERT), totalling  $\sim 640$  MB at  $N_{\text{gridmax}} = 5 \times 10^6$ .

Our recursive  $k$ -section decomposition replaces the one-dimensional Hilbert partitioning with a recursive spatial partitioning in the original three-dimensional coordinate space. This produces a  $k$ -ary tree whose structure directly encodes the communication pattern, enabling hierarchical message routing that scales with the tree depth rather than the total number of ranks.

### 2.2 Hierarchical Partitioning of Spatial and Communication Domain

Given  $N_{\text{cpu}}$  MPI ranks, we first compute the prime factorization as

$$N_{\text{cpu}} = p_1^{m_1} \times p_2^{m_2} \times \cdots \times p_r^{m_r}, \quad p_1 > p_2 > \cdots > p_r. \quad (1)$$

The splitting sequence is then

$$\mathbf{k} = (\underbrace{p_1, \dots, p_1}_{m_1}, \underbrace{p_2, \dots, p_2}_{m_2}, \dots, \underbrace{p_r, \dots, p_r}_{m_r}), \quad (2)$$

yielding  $L (= \sum_i m_i)$  levels in the tree, which encodes both the domain hierarchy and the communication pattern. At each level  $l$ , the domain is split into  $k_l$  sub-domains along the longest axis of the current bounding box. This longest-axis selection ensures roughly isotropic sub-domains, minimising the surface-to-volume ratio and hence the ghost-zone count.

For example,  $N_{\text{cpu}} = 12 = 3 \times 2 \times 2$  produces the splitting sequence  $(3, 2, 2)$  with  $L = 3$  tree levels: the root is split into 3 slabs along the longest axis, each slab is bisected, and each half is bisected again, yielding 12 leaf nodes — one per rank. Figure 1 illustrates this progressive decomposition for  $N_{\text{cpu}} = 12$ , from the undivided domain through three successive levels of splitting, with the corresponding  $k$ -section tree shown beneath each panel.

The tree is stored as a set of arrays indexed by node identifier. For each internal node, the child indices for each of the  $k_l$  partitions and the spatial coordinates of the partition boundaries are recorded; for each leaf node, the assigned MPI rank

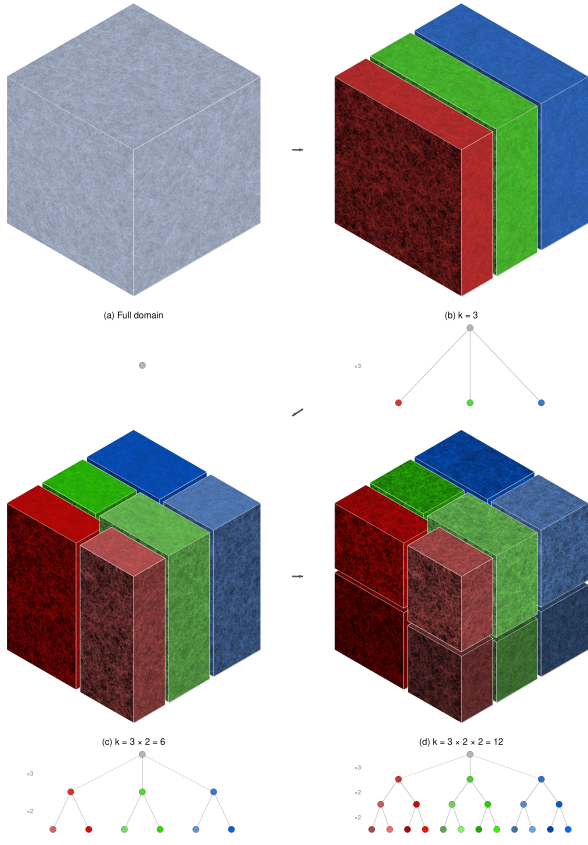


**Figure 1.** Progressive recursive  $k$ -section decomposition for  $N_{\text{cpu}} = 12 = 3 \times 2 \times 2$ . (a) The undivided simulation domain. (b) First split into  $k = 3$  slabs along the longest axis. (c) Each slab bisected along the second axis ( $3 \times 2 = 6$  sub-domains). (d) Final bisection along the third axis ( $3 \times 2 \times 2 = 12$  leaf domains). Below each panel, the corresponding  $k$ -section tree is shown; colours encode  $x$ -slab membership (red/green/blue), with saturation and brightness indicating  $y$  and  $z$  subdivisions. Each face displays projected column density from a  $4096^3$  TSC density field. Sub-domain volumes vary by  $\sim 10\text{--}30\%$ , reflecting load-balanced wall placement.

is stored. Every node also carries the minimum and maximum rank indices of all leaves in its subtree, enabling rapid range queries during the hierarchical exchange.

The total number of tree nodes is

$$N_{\text{nodes}} = 1 + \sum_{l=1}^L \prod_{i=1}^l k_i \leq 1 + L \cdot k_{\max}^L, \quad (3)$$

which for practical values ( $N_{\text{cpu}} \leq 10^5$ ) is at most a few hundred — negligible overhead.

### 2.3 Load-Balanced Wall Placement

When the tree is updated during load balancing (every  $n_{\text{remap}}$  coarse steps), the wall positions are adjusted by iterative dichotomy so that each partition receives a load proportional to the number of ranks it contains.

The procedure operates level by level, top to bottom. At level  $l$ :

(i) A histogram is built over the splitting coordinate: for

each node at level  $l$ , the cells within that node are projected onto the splitting axis and binned into a cumulative cost histogram with resolution  $\Delta x_{\text{hist}}$ .

(ii) For each of the  $k_l - 1$  walls within each node, a binary search (dichotomy) adjusts the wall position until the cumulative load on the left side matches the target fraction. The target cumulative fraction for wall  $j$  in a node spanning ranks  $[i_{\min}, i_{\max}]$  with total count  $n = i_{\max} - i_{\min} + 1$  is

$$f_j = n^{-1} \sum_{m=1}^j n_m, \quad (4)$$

where  $n_m$  is the number of ranks assigned to partition  $m$  ( $n_m = \lfloor n/k_l \rfloor$  or  $\lfloor n/k_l \rfloor + 1$  for the first  $n \bmod k_l$  partitions).

(iii) An MPI\_ALLREDUCE aggregates the local histograms across all  $N_{\text{cpu}}$  ranks to obtain the global cumulative load at each wall position. The dichotomy converges when the relative load imbalance  $|\hat{L}_j - L_j^{\text{target}}|/L_j^{\text{target}}$  falls below a tolerance  $\epsilon_{\text{tol}}$  (typically 1 per cent), or when the wall position can no longer be resolved at the histogram resolution.

(iv) After wall convergence, the cells are repartitioned (sorted) according to the new wall positions, and the histogram bounds are updated for the next level.

### 2.4 Memory-Weighted Cost Function

The default RAMSES load balancer weights all cells equally. cuRAMSES supports an optional memory-weighted cost function:

$$C_{\text{cell}} = 2^{-N_{\text{dim}}} (w_{\text{grid}} + n_{\text{part}}(\text{igrid}) \cdot w_{\text{part}}),$$

where  $w_{\text{grid}}$  is the memory cost per grid slot (default 270 bytes, accounting for hydro, gravity, and AMR bookkeeping arrays),  $w_{\text{part}}$  is the memory cost per particle slot (default 12 bytes for position, velocity, mass, and linked-list pointers), and  $n_{\text{part}}(\text{igrid})$  is the number of particles attached to grid  $\text{igrid}$ . The division by  $2^{N_{\text{dim}}}$  distributes the grid cost evenly among its eight cells.

This cost function ensures that ranks hosting dense haloes (many particles per cell) receive fewer cells, preventing memory exhaustion on particle-heavy ranks. All histogram loads are accumulated in 64-bit integers to avoid overflow when summing costs across millions of cells.

Activating memory-weighted balancing requires setting `memory_balance = .true.` and optionally tuning `mem_weight_grid` and `mem_weight_part` in the namelist. Our tests with 200 M particles on 12 ranks show that memory-weighted balancing reduces the peak-to-mean memory ratio from 2.5 to 1.3 without affecting physics results (identical  $e_{\text{cons}}$ ,  $e_{\text{pot}}$ ,  $e_{\text{kin}}$  to machine precision).

## 3 HIERARCHICAL MPI COMMUNICATION

The tree structure described in Section 2.2 enables a hierarchical exchange protocol that replaces the global MPI\_ALLTOALL with a sequence of level-by-level correspondent exchanges. We implement two variants.

### 3.1 Exclusive Exchange

In the exclusive exchange, each item has a unique destination rank. The algorithm walks the tree from root to leaf:

**Algorithm 1** Exclusive hierarchical exchange

---

**Input:** Send buffer **S** with  $N$  items, destination ranks **d**  
**Output:** Receive buffer **R** with items destined for this rank

```

1: W  $\leftarrow$  S; D  $\leftarrow$  d; node  $\leftarrow$  root
2: for  $l = 1$  to  $L$  do
3:    $k \leftarrow k_l$ ; my_child  $\leftarrow$  ksec_cpu.path(myid,  $l$ )
4:   Classify items in W by child index (counting sort on D)
5:   Identify  $k - 1$  correspondent ranks (one per sibling child)
6:   for each correspondent  $p$  do
7:     Exchange count: MPI_ISEND/IRecv (tag  $100 + l$ )
8:     Exchange data: MPI_ISEND/IRecv (tags  $200 + l$ ,  $300 + l$ )
9:   end for
10:  MPI_WAITALL
11:  W  $\leftarrow$  merge(my_child items, received items)
12:  node  $\leftarrow$  ksec.next(node, my_child)
13: end for
14: R  $\leftarrow$  W

```

---

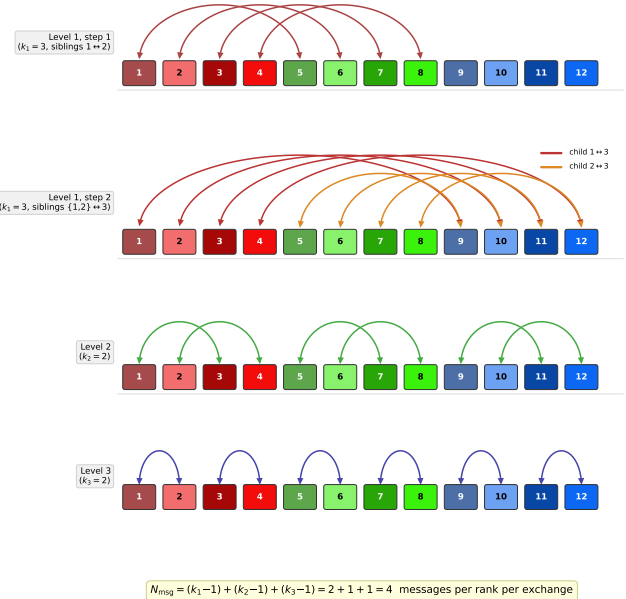
228 At each level, each rank communicates with at most  $k_l - 1$   
229 correspondent ranks (one from each sibling subtree). The  
230 correspondent in a sibling subtree of size  $s$  is chosen as  
231  $\min(\text{my\_pos}, s - 1)$  to distribute load evenly. The total number  
232 of messages per rank per exchange is

$$N_{\text{msg}} = \sum_{l=1}^L (k_l - 1) = \sum_i m_i(p_i - 1), \quad (6)$$

233 which for  $N_{\text{cpu}} = 1024 = 2^{10}$  gives  $N_{\text{msg}} = 10$  — two orders  
234 of magnitude fewer than the  $\sim 1024$  messages required in the  
235 original all-to-all pattern.

236 Figure 2 illustrates the communication pattern for  $N_{\text{cpu}} =$   
237  $12 (= 3 \times 2 \times 2)$ . At level 1 ( $k_1 = 3$ ), the 12 ranks are grouped  
238 into three children of four ranks each. Each rank exchanges  
239 data with one correspondent in each of the two sibling sub-  
240 trees, yielding  $k_1 - 1 = 2$  communication steps: step 1 pairs  
241 children 1 and 2 (e.g. rank 1  $\leftrightarrow$  rank 5), while step 2 sim-  
242 ulaneously pairs children 1 and 3 (dark red arcs, e.g. rank 1  
243  $\leftrightarrow$  rank 9) and children 2 and 3 (orange arcs, e.g. rank 5  $\leftrightarrow$   
244 rank 9). At level 2 ( $k_2 = 2$ ), the scope narrows to within each  
245 group of four, with each rank contacting one correspond-  
246 ent two positions away (e.g. rank 1  $\leftrightarrow$  rank 3). Finally, at level 3  
247 ( $k_3 = 2$ ), only adjacent pairs communicate (e.g. rank 1  $\leftrightarrow$   
248 rank 2). The progressively shorter arcs reflect the hierarchical  
249 narrowing of communication scope: long-range inter-group  
250 exchanges are resolved first, and successive levels refine the  
251 routing within ever-smaller subtrees. Each rank sends a total  
252 of  $N_{\text{msg}} = 2 + 1 + 1 = 4$  messages per exchange, independent  
253 of  $N_{\text{cpu}}$ .

254 The pairing structure at each tree level follows directly  
255 from the branching factor. When a node has  $p$  children, data  
256 from every child must reach every other child. This is accom-  
257 plished in  $p - 1$  sequential steps. In step  $s$  ( $s = 1, \dots, p - 1$ ),  
258 child  $s + 1$  is paired with each of the children  $1, \dots, s$ : each  
259 rank in child  $s + 1$  exchanges data with its correspondent in  
260 child  $c$  for  $c = 1, \dots, s$ , yielding  $s$  concurrent point-to-point  
261 exchanges. After step  $s$ , every child 1 through  $s + 1$  holds  
262 the aggregate of all data originating from children 1 through  
263  $s + 1$ . In particular, after all  $p - 1$  steps, every child possesses  
264

Hierarchical exchange communication pattern for  $N_{\text{cpu}} = 12 (= 3 \times 2 \times 2)$ 

$$N_{\text{msg}} = (k_1 - 1) + (k_2 - 1) + (k_3 - 1) = 2 + 1 + 1 = 4 \text{ messages per rank per exchange}$$

**Figure 2.** Hierarchical exchange communication pattern for  $N_{\text{cpu}} = 12 (= 3 \times 2 \times 2)$ . Coloured rectangles represent MPI ranks numbered 1–12, using the same colour scheme as Figure 1. Arcs denote bidirectional point-to-point exchanges. At level 1 ( $k_1 = 3$ ), two steps connect each rank with correspondents in the two sibling subtrees; the two colours in step 2 distinguish the children 1↔3 (dark red) and children 2↔3 (orange) pairings that proceed concurrently. At levels 2 and 3 ( $k_2 = k_3 = 2$ ), the communication range contracts to within each group and then to adjacent pairs. The total message count per rank is  $N_{\text{msg}} = (3 - 1) + (2 - 1) + (2 - 1) = 4$ .

the complete data set of the entire subtree. For the  $N_{\text{cpu}} = 12$  example in Figure 2, level 1 has  $k_1 = 3$ , giving  $3 - 1 = 2$  steps: step 1 pairs child 2 with child 1 ( $1 \times 4$  exchanges), and step 2 pairs child 3 with both children 1 and 2 ( $2 \times 4$  exchanges). Levels 2 and 3 each have  $k = 2$ , requiring only  $2 - 1 = 1$  step per level.

Working buffers are managed with Fortran 2003 move\_alloc for zero-copy buffer swaps at each level, and per-level arrays (child counts, peer lists, MPI request handles) are pre-allocated with save attributes to eliminate allocation/deallocation overhead on repeated calls.

### 3.2 Ghost-Zone Exchange via K-Section

The ghost-zone (virtual boundary) exchange is the most communication-intensive operation in RAMSES, called multiple times per fine time step for hydro, gravity, and particle updates. We replace the standard all-to-all pattern with four  $k$ -section-based variants. First, a forward exchange sends data from emission grids to reception grids, and a corresponding reverse accumulation adds received values back into the emission grids. Because the hierarchical routing internally uses double-precision buffers, an integer variant packs integer data (e.g. `cpu_map`, `flag1`) into double-precision words

**Table 1.** Communication complexity per ghost-zone exchange operation.  $N_{\text{ghost}}$  is the total number of ghost grids per rank;  $k_l$  are the branching factors at tree level  $l$ .

	Original RAMSES	cuRAMSES
Message count	$\mathcal{O}(N_{\text{cpu}})$	$\mathcal{O}(\sum_l k_l)$
Buffer memory	$\mathcal{O}(N_{\text{cpu}} \cdot N_{\text{ghost}})$	$\mathcal{O}(k_{\max} \cdot N_{\text{ghost}})$
MPI_ALLTOALL calls	$\geq 1$ per exchange	0

before transport and unpacks them on receipt, reusing the same tree-walk machinery without a separate integer communication path.

The data packing format for each ghost grid is:

$$\text{sendbuf}(1 : 2^{N_{\text{dim}}} + 2, i) = \{u_1, \dots, u_{2^{N_{\text{dim}}}}, \text{sender\_id}, \text{index}\}, \quad (7)$$

where  $u_j$  are the cell data values, `sender_id` identifies the source rank, and `index` is the emission or reception array index used for scatter at the receiver. This self-describing format enables the receiver to place incoming data without maintaining separate communication tables.

For multi-variable exchanges (e.g. all hydro conserved variables), we provide bulk variants that pack all  $N_{\text{var}}$  columns of a 2D array into a single  $k$ -section exchange call:

$$\text{sendbuf}((v - 1)2^{N_{\text{dim}}} + j, i) = \text{xx}(v, \text{cell}_{i,j}), \quad (8)$$

for  $v = 1, \dots, N_{\text{var}}$  and  $j = 1, \dots, 2^{N_{\text{dim}}}$ , plus two metadata entries. This amortises the tree-walk overhead and MPI latency over  $N_{\text{var}}$  variables, yielding a significant reduction in the number of exchange calls per time step (from  $N_{\text{var}}$  individual calls to a single bulk call at each of the five call sites in `amr_step`).

### 3.3 Communication Structure Construction

The construction of the communication structure, which determines which grids must be exchanged as ghost zones, was itself based on MPI\_ALLTOALL in the original RAMSES. We replace this with a  $k$ -section exchange: each rank packs its reception grids as triplets (sender identifier, reception index, grid address), sends them via the exclusive hierarchical exchange, and the receiver reconstructs its emission arrays from the incoming data. This eliminates the last remaining all-to-all communication pattern in the AMR infrastructure.

### 3.4 Complexity Analysis

Table 1 summarizes the communication complexity of the original RAMSES and cuRAMSES.

## 4 MORTON KEY OCTREE FOR NEIGHBOUR LOOKUP

### 4.1 The Nbor Array Problem

RAMSES stores the octree connectivity in several arrays, the largest of which is `nbor(1:ngridmax, 1:twodim)` — a six-column integer array that records, for each grid, the cell index of its neighbour in each of the six Cartesian directions ( $\pm x, \pm y, \pm z$ ).

At 8 bytes per entry (64-bit integers), this array consumes

$$M_{\text{nbor}} = 6 \times 8 \times N_{\text{gridmax}} = 48 N_{\text{gridmax}} \text{ bytes.} \quad (9)$$

For  $N_{\text{gridmax}} = 5 \text{ M}$ , this is 240 MB per rank. Moreover, the `nbor` array must be maintained during grid creation, deletion, defragmentation, and inter-rank migration — a significant source of code complexity and a potential source of bugs.

## 4.2 Morton Key Encoding

A Morton key (also known as a Z-order key) is a 64-bit integer formed by interleaving the bits of the three-dimensional integer coordinates  $(i_x, i_y, i_z)$  of a grid at its AMR level:

$$M(i_x, i_y, i_z) = \sum_{b=0}^{B-1} [ \text{bit}_b(i_x) \cdot 2^{3b} + \text{bit}_b(i_y) \cdot 2^{3b+1} + \text{bit}_b(i_z) \cdot 2^{3b+2} ], \quad (10)$$

where  $B = 21$  bits per coordinate (supporting grids up to level 22 for  $n_x = 1$ , or level 20 for  $n_x = 4$ ), and  $\text{bit}_b(n)$  extracts bit  $b$  of integer  $n$ . The encoding and decoding are implemented with simple bit-shift loops.

The integer coordinates of a grid at level  $l$  are computed from its floating-point centre position  $\mathbf{x}_g$  as

$$i_d = \lfloor x_{g,d} \cdot 2^{l-1} \rfloor, \quad d \in \{x, y, z\}, \quad (11)$$

where coordinates are in units of the coarse grid spacing.

## 4.3 Neighbour Finding via Morton Arithmetic

The neighbour of a grid in direction  $j$  (using the RAMSES convention  $1 = -x, 2 = +x, 3 = -y, 4 = +y, 5 = -z, 6 = +z$ ) is obtained by:

- (i) Decoding the Morton key to  $(i_x, i_y, i_z)$ .
- (ii) Incrementing or decrementing the appropriate coordinate.
- (iii) Applying periodic wrapping if the coordinate exceeds  $[0, n_d \cdot 2^{l-1}]$ .
- (iv) Re-encoding to obtain the neighbour’s Morton key.

The parent key is obtained by a 3-bit right shift:  $M_{\text{parent}} = M \gg 3$ . A child key is obtained by a 3-bit left shift plus the child index (0–7):  $M_{\text{child}} = (M \ll 3) | i_{\text{child}}$ .

## 4.4 Per-Level Hash Table

We maintain one open-addressing hash table per AMR level, mapping Morton keys to grid indices:

$$\text{mort\_table}(l) : M \mapsto \text{igrid}. \quad (12)$$

The hash function uses multiplicative hashing with Knuth’s golden ratio constant and an additional mixing step:

$$h(M) = [((M \times \phi_1) \oplus (M \gg 16)) \times \phi_2] \oplus (h \gg 13), \quad (13)$$

where  $\phi_1 = 2654435761$  and  $\phi_2 = 0x9E3779B97F4A7C15$  are constants chosen for good bit mixing, and the table capacity is always a power of two to allow bitmask modular arithmetic. Collisions are resolved by linear probing; the load factor is kept below 0.7 by automatic rehashing (doubling capacity).

The hash table is maintained incrementally:

- 365 • `morton_hash_insert`: called during `make_grid_coarse`  
 366 and `make_grid_fine`;  
 367 • `morton_hash_delete`: called during `kill_grid`;  
 368 • Full rebuild after defragmentation  
 369 (`morton_hash_rebuild`).

370 A companion array `grid_level(igrid)` stores the AMR  
 371 level of each grid, enabling Morton key computation from  
 372 the grid index alone.

#### 373 4.5 Replacement Functions

374 Two wrapper functions provide drop-in replacements for the  
 375 original `nbor`-based access patterns:

- 376 • `morton_nbor_grid(igrid, ilevel, j)`: returns the grid  
 377 index of the same-level neighbour in direction  $j$ , replacing  
 378 the pattern `son(nbor(igrid, j))`. Implemented as: compute  
 379 Morton key, shift by direction, look up in hash table.
- 380 • `morton_nbor_cell(igrid, ilevel, j)`: returns the fa-  
 381 ther cell index of the neighbour, replacing the pattern  
 382 `nbor(igrid, j)`. For level 1, returns the coarse cell index di-  
 383 rectly; for finer levels, computes the parent grid via the hash  
 384 table at level  $l - 1$  and the octant index from the coordinate  
 385 parity.

386 The `nbor` array is reduced to `allocate(nbor(1:1, 1:1))`  
 387 — effectively eliminated while maintaining compilation com-  
 388 patibility with any remaining references.

#### 389 4.6 Memory and Performance Analysis

390 The memory cost of the hash table is

$$M_{\text{hash}} \approx \frac{N_{\text{grids}}}{0.7} \times (8 + 4) \text{ bytes} \approx 17 N_{\text{grids}} \text{ bytes}, \quad (14)$$

391 where  $N_{\text{grids}}$  is the actual number of grids (typically much less  
 392 than  $N_{\text{gridmax}}$ ), 8 bytes per key, 4 bytes per grid index, and a  
 393 load factor of 0.7 accounts for empty slots. The `grid_level`  
 394 array adds  $4 \times N_{\text{gridmax}}$  bytes.

395 Compared to the original `nbor` cost of  $48 \times N_{\text{gridmax}}$  bytes,  
 396 the net savings are

$$\Delta M = 48 N_{\text{gridmax}} - 4 N_{\text{gridmax}} - 17 N_{\text{grids}} \approx 44 N_{\text{gridmax}} - 17 N_{\text{grids}} \quad (15)$$

397 Since  $N_{\text{grids}} \ll N_{\text{gridmax}}$  in practice (typical occupancy is  
 398 30–60 per cent), the savings are substantial:  $\sim 176 \text{ MB}$  for  
 399  $N_{\text{gridmax}} = 5 \text{ M}$  at 50 per cent occupancy.

400 The computational cost of a hash lookup is  $\mathcal{O}(1)$  expected  
 401 time, with worst-case linear probing bounded by the load  
 402 factor. In practice, the precomputed neighbour caches de-  
 403 scribed in Section 6 amortize any per-lookup overhead in the  
 404 performance-critical Poisson solver.

#### 405 5 MEMORY OPTIMIZATIONS

406 Beyond the Morton key hash table, several additional opti-  
 407 mizations reduce the steady-state memory footprint.

**Table 2.** Memory savings per MPI rank for  $N_{\text{gridmax}} = 5 \text{ M}$ . Savings marked with \* are conditional on using  $k$ -section ordering.

Optimization	Savings (MB)	Availability
<code>nbor</code> elimination (Morton hash)	240	Always
<code>hilbert_key</code> elimination*	640	Steady state
On-demand <code>bisec_ind_cell</code> *	160	Between LB steps
On-demand <code>cell_level</code> *	160	Between LB steps
Defrag scratch (local)	40	Between defrag
<b>Total</b>	<b>&gt;1200</b>	

#### 5.1 Hilbert Key Elimination

When using  $k$ -section ordering, the Hilbert key array `hilbert_key(1:nccell)` is no longer needed for domain decomposition. We replace it with `allocate(hilbert_key(1:1))`, saving

$$\Delta M_{\text{hilbert}} = 16 \times N_{\text{gridmax}} \times 2^{N_{\text{dim}}} \text{ bytes} \quad (16)$$

under QUADHILBERT (128-bit keys stored as two 64-bit integers). For  $N_{\text{gridmax}} = 5 \text{ M}$ , this is approximately 640 MB.

The defragmentation routine, which previously required Hilbert keys for reordering, uses a local scratch array (`defrag_dp`) allocated only during the defragmentation pass and immediately deallocated.

#### 5.2 On-Demand Histogram Arrays

The arrays `bisec_ind_cell` and `cell_level`, each of size  $N_{\text{gridmax}} \times 2^{N_{\text{dim}}}$  integers (8 bytes), are used exclusively during load balancing to build the bisection histogram. We allocate them on entry to `init_bisection_histogram` and deallocate them after `cmp_new_cpu_map` returns. The savings are

$$\Delta M_{\text{hist}} = 2 \times 8 \times N_{\text{gridmax}} \times 2^{N_{\text{dim}}} \approx 320 \text{ MB} \quad (17)$$

for  $N_{\text{gridmax}} = 5 \text{ M}$ . Since load balancing occurs only every `nremap` coarse steps, these arrays are absent during the vast majority of the simulation.

#### 5.3 Memory Savings Summary

Table 2 summarizes the memory savings for  $N_{\text{gridmax}} = 5 \text{ M}$ .

The reported memory savings of the `nbor` array account for both the eliminated array ( $48 N_{\text{gridmax}} = 240 \text{ MB}$ ) and the hash table overhead ( $\sim 17 N_{\text{grids}}$ , typically  $< 50 \text{ MB}$ ). Net savings are at least 190 MB. The Hilbert key savings of 640 MB assume QUADHILBERT; for standard 64-bit keys the savings would be 320 MB.

We implement a diagnostic routine `writemem_minmax` that reports the minimum and maximum resident set size across all ranks at each coarse step, providing runtime verification of the memory savings.

## 6 MULTIGRID POISSON SOLVER OPTIMIZATIONS

The multigrid (MG) Poisson solver consumes a large fraction of the total runtime in self-gravitating cosmological simulations. In baseline RAMSES, profiling reveals that the MG solver accounts for approximately 55 per cent of the total

447 wall-clock time per coarse step. We describe several optimiza- 496  
 448 tions that reduce this fraction to approximately 39 per cent. 497

### 499 6.1 Neighbour Grid Precomputation

500 The Gauss–Seidel (GS) smoother and residual computation 501  
 501 both require access to the six Cartesian neighbours of each 502 grid. In the Morton hash table approach (Section 4), each 503 neighbour lookup involves a hash table query. While individual 504 lookups are  $\mathcal{O}(1)$ , the GS kernel accesses 6 neighbours 505 per grid, 8 cells per grid, and typically 4–5 V-cycle iterations, 506 resulting in hundreds of hash lookups per grid per solve.

507 We precompute all neighbour grids into a contiguous array 506 before entering the V-cycle iteration loop:

$$\text{nbor\_grid\_fine}(j, i) = \text{morton\_nbor\_grid}(\text{igrid\_amr}(i), l, j), \quad (18)$$

459 for  $j = 0, 1, \dots, 6$  (where  $j = 0$  stores the grid’s own AMR 460 index `igrid_amr`) and  $i = 1, \dots, N_{\text{grid}}$ . This array is allocated 461 before the iteration loop and deallocated after, so its memory 462 overhead is transient.

### 463 6.2 Branch-Free Neighbour Access

464 The original GS kernel contains a branch on `igshift == 513`  
 465 0 to distinguish between the current grid and its neig- 514  
 466 bours. We unify the access pattern with a cache array 515  
 467 `nbor_grids_cache(0:twondim)`, where index 0 references the 516 grid itself. All neighbour accesses — including the self- 517 reference — use the same indexed load, eliminating the 518 branch.

### 471 6.3 Merged Red-Black Exchange

472 Standard red-black Gauss–Seidel smoothing in RAMSES per- 520  
 473 forms a ghost-zone exchange of the potential  $\phi$  between the 521 red and black sweeps:

$$\text{Red} \rightarrow \text{Exchange}(\phi) \rightarrow \text{Black} \rightarrow \text{Exchange}(\phi). \quad (19)$$

475 Each iteration thus requires two exchanges for the smoother 524  
 476 alone, plus additional exchanges for the residual and restric- 525  
 477 tion/prolongation steps — a total of 9 exchange calls per 526  
 478 iteration.

479 We merge the red and black sweeps by removing the inter- 528  
 480 sweep exchange:

$$\text{Red} \rightarrow \text{Black} \rightarrow \text{Exchange}(\phi). \quad (20)$$

481 This is a form of *chaotic relaxation*: boundary cells in the 531  
 482 black sweep use slightly stale ghost values from the previ- 532  
 483 ous iteration rather than freshly exchanged red-sweep values. 533  
 484 For the MG preconditioner, this does not affect convergence 534  
 485 in practice — the MG solve is itself an approximate precon- 535  
 486 ditioner for the conjugate gradient outer iteration, and the 536  
 487 stale-ghost error is well within the MG tolerance.

488 We also remove two unnecessary residual exchanges per 537  
 489 iteration, reducing the total from 9 to 5 exchange calls per 538  
 490 iteration — a 44 per cent reduction in MG communication 539  
 491 volume.

492 The same optimization is applied to the coarse-level 538  
 493 solver (direct solve, pre-smoothing, post-smoothing), where 539  
 494 the merged red-black pattern similarly halves the exchange 540  
 495 count.

### 6.4 Fused Residual and Norm Computation

The MG algorithm requires both the residual  $r = f - A\phi$  and its  $L^2$  norm  $\|r\|_2^2$  at specific points in the V-cycle. In the original code, these are computed in separate passes. We add an optional `norm2` argument to `cmp_residual_mg_fine`: when present, the norm is accumulated during the same loop that computes the residual, saving one full grid traversal.

Since the subroutine is `external` (not module-contained), callers must include an `interface` block to enable the optional-argument dispatch.

### 6.5 Arithmetic Optimization

The GS fast-path computation involves a division by  $2N_{\text{dim}} = 6$ :

$$\phi_{\text{new}} = \frac{\sum_j \phi_j - h^2 f}{2N_{\text{dim}}}. \quad (21)$$

We replace the division / `dwtwondim` with a multiplication by the precomputed reciprocal \* `oneoverdtwondim`, which is faster on most architectures.

### 6.6 Performance Impact

Combining all optimizations, the MG Poisson solver’s share of total runtime is reduced from 55.1 per cent to 38.6 per cent in a representative test (200 M particles, 12 ranks, 10 coarse steps). The iteration counts are unchanged (Level 8: 5 iterations, Level 9: 4 iterations), confirming that the merged red-black exchange does not degrade convergence.

## 7 FEEDBACK SPATIAL BINNING

### 7.1 The Brute-Force Bottleneck

The Type II supernova (SNII) feedback implementation in RAMSES involves two computationally expensive routines:

- `average_SN`: averages hydrodynamic quantities within the blast radius of each SN event, accumulating volume, momentum, kinetic energy, mass loading, and metal loading. The original implementation loops over all cells  $\times$  all SNe, yielding  $\mathcal{O}(N_{\text{cells}} \times N_{\text{SN}})$  complexity.

- `Sedov_blast`: injects the blast energy and ejecta into cells within the blast radius. Same  $\mathcal{O}(N_{\text{cells}} \times N_{\text{SN}})$  complexity.

In production simulations with  $\sim 2000$  simultaneous SN events, these routines consume 66 s and 11 s per call respectively, dominating the feedback time step.

### 7.2 Spatial Hash Binning

We partition the simulation domain into a uniform grid of  $n_{\text{bin}}^3$  bins, where

$$n_{\text{bin}} = \max(1, \min(128, \lfloor L_{\text{box}}/r_{\text{max}} \rfloor)), \quad (22)$$

and  $r_{\text{max}}$  is the maximum SN blast radius (the larger of `rcell`  $\times$  `dx_min` and `rbubble`). Each SN event is assigned to a bin based on its position, and a linked list threads the events within each bin:

$$\text{bin\_head}(i_x, i_y, i_z) \rightarrow \text{SN}_1 \rightarrow \text{SN}_2 \rightarrow \dots \quad (23)$$

For each cell, we compute its bin index and check only the 27 neighbouring bins (the cell's own bin plus its 26 face-, edge-, and corner-adjacent bins). Since  $r_{\max}$  is at most the bin size, by construction, this 27-bin neighbourhood is guaranteed to contain all SNe that could influence the cell. The complexity becomes

$$\mathcal{O}(N_{\text{cells}} \times \bar{n}_{\text{SN/bin}} \times 27), \quad (24)$$

where  $\bar{n}_{\text{SN/bin}} = N_{\text{SN}}/n_{\text{bin}}^3$  is the average number of SNe per bin.

### 7.3 Parallelization

#### 7.3.1 Cell-parallel average\_SN

The binned `average_SN` uses cell-parallel OpenMP threading: the outer loop is over grids (with `!$omp parallel do`), and each thread processes the cells of one grid. When a cell falls within an SN blast radius, the thread accumulates its contribution using `!$omp atomic` directives on the shared SN-indexed arrays (`vol_gas`, `dq`, `ekBlast`, etc.). The atomic overhead is minimal because collisions are rare — most bins contain zero or one SN, so contention is low.

#### 7.3.2 Grid-parallel Sedov\_blast

The `Sedov_blast` routine writes only to cells owned by each grid, so no atomics are needed. The outer loop is over grids, and each thread independently processes the cells of its assigned grids, checking only the 27 neighbouring bins for relevant SNe.

### 7.4 Performance Results

With approximately 2000 simultaneous SN events:

- `average_SN`: 66 s → 0.25 s ( $\sim 260\times$  speedup)
- `Sedov_blast`: 11 s → 0.07 s ( $\sim 157\times$  speedup)

Verification by restarting at the same snapshot confirms bit-identical results for all conservation quantities ( $m_{\text{cons}}$ ,  $e_{\text{cons}}$ ,  $e_{\text{pot}}$ ,  $e_{\text{kin}}$ ,  $e_{\text{int}}$ ).

### 7.5 AGN Feedback Spatial Binning

The same spatial binning technique is applied to the AGN feedback routines (`average_AGN` and `AGN_blast`), which suffer from the same  $\mathcal{O}(N_{\text{cells}} \times N_{\text{AGN}})$  brute-force scaling. In production simulations with tens of thousands of active AGN sink particles, these routines dominate the sink-particle time step.

The AGN feedback involves three distinct interaction modes (saved energy injection, jet feedback, and thermal feedback), each with a different geometric distance criterion. The spatial binning is agnostic to these distinctions: it reduces the candidate AGN set from the full population to only those in the 27 neighbouring bins, while preserving all distance-check logic and physical calculations unchanged. The linked-list construction and 27-bin traversal follow the same pattern as the SNII implementation (§7.2), with `bin_head` and `agn_next` arrays replacing the SN-specific versions.

With approximately 32 000 active AGN particles, the binned `average_AGN` achieves a  $30\times$  speedup and `AGN_blast` a  $14\times$  speedup, reducing the total AGN feedback time by a factor of  $\sim 4$ . Verification confirms bit-identical conservation diagnostics compared to the original brute-force implementation.

## 8 VARIABLE-NCPU RESTART AND OTHER IMPROVEMENTS

### 8.1 HDF5 Parallel I/O

Standard RAMSES writes one binary file per MPI rank per output. Restarting with a different number of ranks is not directly supported, requiring an intermediate step of reading with the original rank count, redistributing, and re-writing.

We implement HDF5 parallel I/O using the HDF5 library's MPI-IO backend. All ranks write to (and read from) a single HDF5 file, with datasets organized hierarchically:

- `/amr/level_{1}/`: grid positions, son flags, CPU map for each AMR level.
- `/hydro/level_{1}/`: conserved variables  $\rho$ ,  $\rho\mathbf{v}$ ,  $E$ , etc.
- `/gravity/level_{1}/`: gravitational potential  $\phi$  and force components.
- `/particles/`: positions, velocities, masses, IDs, levels, formation times, metallicities.
- `/sinks/`: sink particle properties.

### 8.2 Variable-Ncpu Restart Algorithm

When the number of ranks in the output file ( $N_{\text{cpu}}^{\text{file}}$ ) differs from the current run ( $N_{\text{cpu}}$ ), the following procedure executes during restart:

- (i) Build a uniform  $k$ -section tree for the new  $N_{\text{cpu}}$  (equal-volume partitioning, without load-balance adjustment).
- (ii) Read all grids from the HDF5 file. Since the file is a single shared file, all ranks can access all data.
- (iii) For each grid, compute the CPU ownership from the father cell's position using `cmp_ksection_cpumap`.
- (iv) Each rank retains only the grids assigned to it, building the local AMR tree incrementally.
- (v) Hydro, gravity, and particle data are read and scattered to locally owned grids using a precomputed file-index-to-local-grid mapping (`varcpu_grid_file_idx`).
- (vi) On the first coarse step after restart, a forced load-balance operation redistributes grids for optimal balance under the new rank configuration.

This approach requires that all ranks temporarily hold the full grid metadata (positions and son flags) during the reconstruction phase. For typical production outputs ( $\sim 10$  M total grids), this temporary overhead is a few hundred MB — well within the memory budget freed by the optimizations of Sections 4–5.

### 8.3 Binary Distributed I/O Restart

When HDF5 is unavailable or the native binary format (`informat='origin'`) is preferred, a distributed I/O strategy enables variable- $N_{\text{cpu}}$  restart from the per-rank binary files written by standard RAMSES. The binary for-

mat stores one file per MPI rank — `amr_XXXXX.outYYYYY`, `hydro_XXXXX.outYYYYY`, etc. — so the number of files equals  $N_{\text{cpu}}^{\text{file}}$ , which may differ from the current  $N_{\text{cpu}}$ .

The restart proceeds in three stages.

#### 8.3.0.1 Stage 1: Early detection and file assignment.

Rank 1 probes the header of file 00001 to read  $N_{\text{cpu}}^{\text{file}}$ . If  $N_{\text{cpu}}^{\text{file}} \neq N_{\text{cpu}}$ , the variable- $N_{\text{cpu}}$  path is activated (requiring  $k$ -section ordering). The  $N_{\text{cpu}}^{\text{file}}$  files are distributed among the  $N_{\text{cpu}}$  ranks by round-robin assignment: rank  $r$  reads files whose index satisfies  $(f - 1) \bmod N_{\text{cpu}} = r - 1$ .

#### 8.3.0.2 Stage 2: Distributed AMR reconstruction.

Each rank reads only its assigned AMR files, extracting per-level active grid metadata (positions  $\mathbf{x}_g$  and son flags). The per-level active grid counts are aggregated via `MPI_ALLREDUCE`. For each level, the grids read by each rank are assigned to their correct owner by evaluating `cmp_ksection_cpumap` on the father cell position (computed from  $\mathbf{x}_g$  and the parent-child octant relationship). An `MPI_ALLTOALLV` exchange then routes each grid's data to its owner, who creates the local AMR grid. The exchange metadata — send ordering and receive-grid mapping — is stored for reuse.

#### 8.3.0.3 Stage 3: Hydro and gravity scatter.

The hydro and gravity binary files are read in the same distributed fashion: each rank reads only its assigned files and packs the cell-centred data into per-level send buffers using the stored send ordering. The same `MPI_ALLTOALLV` counts and displacements from Stage 2 are reused, and the receive-grid mapping scatters incoming data to the correct local cells. Since the binary format stores primitive variables (density, velocity, pressure), a primitive-to-conservative conversion is applied on the receiving side.

Particle files are handled independently: each rank reads its assigned files and retains only those particles whose positions fall within the local  $k$ -section domain.

This three-stage approach ensures that no rank reads more than  $\lceil N_{\text{cpu}}^{\text{file}} / N_{\text{cpu}} \rceil$  files (at most two for practical configurations), and the `MPI_ALLTOALLV` exchange per level has cost proportional to the number of grids exchanged rather than the total number of ranks. Verification tests confirm  $e_{\text{cons}} = 0$  for both upward ( $4 \rightarrow 12$ ) and downward ( $12 \rightarrow 4$ ) rank-count changes.

### 8.4 Stream-Access IC Reading

The initial condition (IC) files in GRAFIC2 format are Fortran sequential-access binary files. In the original RAMSES, each rank reads the entire file sequentially, skipping planes until reaching its assigned region. For large ICs, this sequential skipping becomes a significant I/O bottleneck.

We replace sequential access with Fortran 2003 stream access (`ACCESS='STREAM'`), which allows direct byte-offset positioning. The byte offset for plane  $i$  in a file with header size  $H = 52$  bytes (GRAFIC2 44-byte header plus record markers) and plane size  $P = n_1 n_2 \times 4 + 8$  bytes (data plus two 4-byte record markers) is

$$\text{offset} = H + (i - 1) \times P + 5. \quad (25)$$

This is applied to all IC file types: density perturbation

**Table 3.** Effect of `nremap` on total runtime and load-balance overhead. All configurations produce identical physics results ( $e_{\text{cons}} = 3.77 \times 10^{-3}$  at step 10).

<code>nremap</code>	Total (s)	LB time (s)	LB fraction
1	303.8	64.4	21.2%
3	269.9	24.7	9.1%
5	249.8	15.7	6.3%
10	258.6	11.6	4.5%

(`deltab`), velocity components (`velcx/y/z`), particle positions (`poscx/y/z`), and temperature.

## 8.5 Sink Particle Refinement Fix

We identified and fixed a bug in the sink particle refinement criterion. The original implementation in `cic_amr` added the refinement mass threshold `m_refine` to the gravitational potential array `phi`. However, the Poisson solver subsequently overwrites `phi`, erasing the refinement flag.

The fix moves the sink-particle refinement check to `sub_userflag_fine` in `flag_utils`, where it is evaluated after the Poisson solve. For each grid, the particle linked list is traversed once to build a bitmask indicating which child cells contain sink particles (identified by `idp < 0` and `tp = 0`). The cell assignment is determined by comparing the particle position to the grid centre to identify the octant. After calling `poisson_refine`, cells flagged in the bitmask are forced to refine regardless of the Poisson criterion.

## 9 ADDITIONAL IMPLEMENTATION DETAILS

### 9.1 Nremap Tuning

The parameter `nremap` controls the frequency of load-rebalancing operations (every `nremap` coarse steps). We changed the default from `nremap = 0` (rebalance every step) to `nremap = 5` based on systematic tests with 200 M particles on 12 ranks over 10 coarse steps:

The optimal value `nremap = 5` balances the cost of rebalancing against the growing imbalance that accumulates between rebalancing steps. Higher values (`nremap = 10`) reduce LB overhead further but allow imbalance to grow enough to slow other operations, resulting in a net increase in total runtime.

### 9.2 Load-Balance Profiling

To identify bottlenecks in the load-balancing procedure, we added internal timing instrumentation that reports the wall-clock time of each phase:

- (i) `numbp_sync`: MPI synchronization of particle counts for virtual grids.
- (ii) `cmp_new_cpu_map`: histogram construction and wall finding.
- (iii) `expand_pass`: ghost-zone expansion after grid migration.
- (iv) `grid_migration`: actual grid transfer between ranks.
- (v) `allreduce+cpumap_update`: global reduction and CPU map reconstruction.

741 (vi) `shrink_pass`: removal of migrated grids from source rank. 793  
 742 Profiling reveals that `allreduce+cpumap_update` dominates, consuming approximately 50 per cent of the total load- 794  
 743 balance time. This motivates the `nremap = 5` default, as reducing the frequency of these expensive global operations has 795  
 744 a disproportionate impact on total runtime. 796  
 745  
 746

### 9.3 Pre-Allocated Buffer Pools

749 The  $k$ -section exchange routines and virtual boundary functions contain numerous small arrays (child counts, peer lists, 800  
 750 MPI request handles, receive buffers) that are allocated and 801  
 751 deallocated on every call. At 100+ calls per time step, the 802  
 752 cumulative allocation overhead becomes non-negligible. 803  
 753

754 We convert these to `save` variables with grow-only semantics: the buffer is allocated on first use and grown (but never 804  
 755 shrunk) when a larger size is needed. The receive buffer's first 805  
 756 dimension must match the `nprops` parameter exactly (for cor- 806  
 757 rect MPI stride), so reallocation is triggered when either the 807  
 758 capacity or the property count changes. 808  
 759

760 This optimization eliminates approximately 100 alloca- 811  
 761 tion/deallocation pairs per exchange call. 812

## 10 HYBRID CPU/GPU DISPATCH

762 Certain compute-intensive routines—the Godunov solver, 812  
 763 gravity force computation, hydrodynamic synchronisation, 813  
 764 CFL timestep, prolongation, and radiative cooling—are 814  
 765 amenable to GPU acceleration. Rather than offloading en- 815  
 766 tire time steps to the GPU, `CURAMSES` adopts a *hybrid* 816  
 767 *dispatch* model in which OMP threads dynamically choose 817  
 768 between CPU and GPU execution at runtime. 818

### 10.1 Dynamic Dispatch Model

770 At the start of each parallel region, each OMP thread at- 824  
 771 tempts to acquire a GPU stream slot via an atomic counter. 825  
 772 Threads that succeed accumulate grid data into a **super-** 826  
 773 **batch buffer** of configurable size (typically 4096 grids) and 827  
 774 launch GPU kernels asynchronously when the buffer is full. 828  
 775 Threads that do not acquire a slot execute the standard CPU 829  
 776 code path. The `schedule(dynamic)` clause ensures load bal- 830  
 777 ancing: if a GPU thread is waiting for kernel completion, 831  
 778 remaining loop iterations are picked up by CPU threads. 832  
 779

780 This design requires no code duplication—the CPU path 830  
 781 is the original Fortran subroutine, and the GPU path is an 831  
 782 alternative branch within the same `!$omp do` loop. 832

### 10.2 Superbatch Buffering and Scatter-Reduce

783 GPU kernel launch latency ( $\sim 10\text{--}50\ \mu\text{s}$ ) is amortised by 836  
 784 batching: each GPU thread accumulates the full stencil data 837  
 785 for many grids before launching a single kernel covering all 838  
 786 accumulated grids. For the Godunov solver, the GPU pipeline 839  
 787 executes five kernels in sequence: primitive variable conver- 840  
 788 sion, slope computation, Riemann tracing, flux computation, 841  
 789 and artificial diffusion. 842

791 A key optimisation is the on-device **scatter-reduce** kernel 841  
 792 that computes the conservative update entirely on the GPU. 842

Instead of transferring the full flux array back to the host ( $\sim 98\text{ MB}$  per flush), the kernel reduces fluxes into compact per-grid output arrays, reducing the device-to-host transfer to  $\sim 5\text{ MB}$  per flush—a  $20\times$  reduction in PCIe bandwidth.

### 10.3 Lock-Free Level $L-1$ Update

The Godunov solver updates conservative variables at both the current level  $L$  and the coarser level  $L-1$ . Level  $L$  writes are conflict-free by construction (each grid maps to unique cell indices), but level  $L-1$  writes can conflict when multiple fine grids share the same coarse parent cell. The original code serialised both levels with `!$omp critical`, destroying all OMP parallelism in the scatter phase.

We eliminate this lock entirely: level  $L$  results are written directly to `unew`, while each thread appends level  $L-1$  flux contributions to a private scatter buffer. After the parallel region, a serial merge applies all buffered entries. The merge cost is negligible ( $< 0.01\text{ s}$  in all tests), and the result is exact—no approximation or race condition.

### 10.4 Fortran–CUDA Interface

The Fortran–CUDA interface uses a two-layer design: a C binding layer (`bind(C)` with `type(c_ptr)` arguments) and a Fortran wrapper layer that converts assumed-size arrays to C pointers via `c_loc`. The assumed-size pattern avoids Fortran array descriptors, which can produce incorrect addresses with certain compilers (notably Intel ifx).

### 10.5 Performance

The GPU-accelerated code produces bit-identical physics results compared to the CPU-only build. On an RTX 5000 Ada GPU with 4 MPI ranks  $\times$  2 OMP threads, the Godunov solver is accelerated by 16 per cent ( $22.0\text{ s} \rightarrow 18.4\text{ s}$ ). The overall speedup is modest because the host-to-device transfer currently dominates (50 per cent of GPU time), leaving significant room for future optimisation via persistent device-side data structures.

## 11 PERFORMANCE RESULTS

### 11.1 Test Configuration

All tests use a cosmological  $\Lambda\text{CDM}$  simulation with  $200\text{ M}$  dark matter particles in a periodic box of side  $256\ h^{-1}\text{ Mpc}$ , initialised at  $z = 29.5$  with MUSIC (Hahn & Abel 2011). The base AMR grid is  $256^3$  (`levelmin=8`) with adaptive refinement up to `levelmax=10`. The simulation is restarted from an HDF5 output at coarse step 5 and evolved to step 10 (5 coarse steps). The test platform is a dual-socket AMD EPYC 7543 node (64 physical cores, 128 threads) with 1 TB of DDR4 memory.

### 11.2 Conservation Verification

All modifications are verified to preserve physical consistency by comparing conservation diagnostics between the modified code and a reference run:

The slight change in  $e_{\text{cons}}$  for the MG-optimized version

**Table 4.** Conservation diagnostics at step 10 for various configurations. All values are identical to the reference within machine precision.

Configuration	$e_{\text{cons}}$	$e_{\text{pot}}$	$e_{\text{kip}}$
Reference (Hilbert)	$3.77 \times 10^{-3}$	$-1.88 \times 10^{-6}$	$1.23 \times 10^{-10}$
K-section (no membal)	$3.77 \times 10^{-3}$	$-1.88 \times 10^{-6}$	$1.23 \times 10^{-10}$
K-section (membal)	$3.77 \times 10^{-3}$	$-1.88 \times 10^{-6}$	$1.23 \times 10^{-10}$
Morton hash + ksection	$3.77 \times 10^{-3}$	$-1.88 \times 10^{-6}$	$1.23 \times 10^{-10}$
MG optimisations	$3.79 \times 10^{-3}$	$-1.88 \times 10^{-6}$	$1.23 \times 10^{-10}$

elapsed time and per-component timer values as a function of  $N_{\text{cpu}}$  on a log–log scale. All major components follow the ideal scaling line closely up to  $\sim 16$  ranks, with gradual deviation at higher rank counts due to communication overhead. Panel (b) shows the speedup relative to the single-rank baseline: parti-

cle operations and the flag routine achieve near-ideal scaling, while the elapsed time reaches  $33.9\times$  at 64 ranks.

#### 11.4 Memory-Weighted Load Balancing

The memory-weighted cost function (equation 5) assigns  $w_{\text{grid}} = 270$  bytes per grid cell and  $w_{\text{part}} = 12$  bytes per particle. Table 6 quantifies the load balance achieved by this scheme across the strong-scaling runs described in the preceding section.

The memory-weighted balancer keeps the per-rank memory imbalance remarkably low:  $M_{\text{max}}/M_{\text{min}} \leq 1.05$  for all rank counts tested, from 2 to 64. This is achieved despite substantial grid-count imbalance at the most populated refined level (level 10, containing 19.5 M grids), where the per-rank max/min ratio grows from 1.13 at 2 ranks to 1.61 at 64 ranks because the  $k$ -section sub-domains become smaller relative to the AMR clustering scale.

The low memory imbalance is key for production runs because each rank must pre-allocate arrays sized to its local  $N_{\text{gridmax}}$ ; a high imbalance forces over-allocation on lightly loaded ranks. With memory-weighted balancing, the 64-rank run requires only 8.6 Gb per rank at peak, compared with the 147.2 Gb needed in a single-rank run — a factor of 17.1 reduction, close to the ideal  $64\times$  scaling modulo the  $\sim 4$  Gb fixed per-rank overhead (MPI buffers, hash tables, coarse grid). The fixed overhead explains why per-rank memory saturates at  $\sim 8$  Gb for 48 and 64 ranks.

The load-balance remap itself costs 16–26 s for  $N_{\text{cpu}} \geq 8$  (Table 5), growing from 2.3 to 5.1 per cent of the total runtime as the computation shrinks under strong scaling — a modest price for near-perfect memory balance.

### 11.3 Strong Scaling

We measure strong scaling by restarting a production-grade cosmological simulation from an HDF5 output. The test problem comprises 54 M AMR grids (levels 9–14) and 135.7 M particles including  $3.2 \times 10^4$  sink particles, with full physics enabled (radiative cooling, star formation, SNII/AGN feedback). The output was written at coarse step 241 with 12 MPI ranks; we run 2 additional coarse steps to step 243. The variable- $N_{\text{cpu}}$  restart feature (§8) allows the output to be read with any number of MPI ranks; a forced `load_balance` on the first coarse step ensures optimal grid distribution before timing begins. The test platform has two AMD EPYC 7543 processors (64 cores, 128 threads) and 1 TB of shared memory; all runs use `OMP_NUM_THREADS=1`.

Table 5 summarises the wall-clock time and per-component timer averages for  $N_{\text{cpu}} = 1$ –64. The elapsed time is the total wall-clock time including HDF5 I/O and load balancing. All configurations yield energy conservation errors  $e_{\text{cons}}$  of  $\mathcal{O}(10^{-4})$ , with small variations due to floating-point summation order changes across different domain decompositions.

Several scaling trends are evident:

- *Particle operations* scale nearly ideally from 1 to 64 ranks: 538 s  $\rightarrow$  14 s, a  $38.4\times$  speedup for  $64\times$  the ranks.
- *Multigrid Poisson solver* dominates the total time ( $\sim 37\%$ ), scaling from 4034 s (1 rank) to 106 s (64 ranks). The 38.2 $\times$  speedup is near-ideal, reflecting the effectiveness of the Morton hash-based neighbour lookup and precomputed cache arrays.
- *Godunov solver* scales 58.4 $\times$  from 1 to 64 ranks (2536 s  $\rightarrow$  43 s). The super-linear speedup arises because multi-rank runs benefit from cache effects: each rank processes a smaller working set that fits in the L3 cache.
- *Sink particle operations* scale well up to 24 ranks (1346 s  $\rightarrow$  69 s, 19.5 $\times$ ) but slow beyond 32 ranks due to the global ALLREDUCE operations in AGN feedback.
- *Load balancing* overhead converges to  $\sim 16$  s beyond 32 ranks. This cost is amortised over `nremap` coarse steps (every 5 steps in production).
- The *overall speedup* reaches  $33.9\times$  at 64 ranks relative to the single-rank baseline, demonstrating excellent scaling efficiency (53%) on this shared-memory node.

Figure 3 visualises these trends. Panel (a) shows the

## 12 CONCLUSIONS

We have presented cuRAMSES, a set of algorithmic and implementation improvements to the RAMSES cosmological AMR code that collectively address the key scaling bottlenecks — communication overhead, memory consumption, solver efficiency, and hardware utilisation — encountered in large-scale cosmological simulations. While previous efforts such as OMP-RAMSES (Lee et al. 2021) and RAMSES-yOMP (Han et al. 2026) introduced MPI+OpenMP hybrid parallelism, cuRAMSES extends this to a three-level MPI+OpenMP+CUDA paradigm suited to the GPU-dominated architectures of current and upcoming exascale supercomputers. The main contributions are:

- (i) **Recursive  $k$ -section domain decomposition.** A recursive  $k$ -ary spatial partitioning that replaces Hilbert curve ordering and enables hierarchical MPI communication with  $\mathcal{O}(\sum_l k_l)$  messages per exchange, eliminating all MPI\_ALLTOALL calls. The tree structure also provides a natural framework for memory-weighted load balancing, which reduces peak-to-mean memory imbalance from 2.5 to 1.3 in particle-heavy simulations.

**Table 5.** Strong scaling results for the CURAMSES code on a dual-socket AMD EPYC 7543 node (64 cores, 1 TB RAM). The test problem has 54 M grids and 135.7 M particles with full physics (cooling, star formation, sink particles, AGN feedback). Elapsed is the total wall-clock time; timer values are per-rank averages. Speedup  $S$  is relative to the single-rank elapsed time.

$N_{\text{cpu}}$	Elapsed (s)	$S$	MG (s)	Godunov (s)	Sinks (s)	Poisson (s)	Particles (s)	Feedback (s)	Flag (s)	Load Bal. (s)	Cooling (s)
1	8181.5	1.0	4034.1	2536.4	1345.5	1130.1	538.3	210.7	161.3	26.4	158.9
2	4253.1	1.9	2152.5	1218.0	656.1	584.7	272.0	107.3	83.5	83.7	79.7
4	2150.9	3.8	1084.6	612.1	312.4	295.0	134.9	53.3	41.5	50.9	41.0
8	1138.6	7.2	558.4	293.9	171.9	159.1	73.9	27.8	21.2	33.0	21.5
12	793.3	10.3	387.3	198.6	131.3	107.4	51.6	20.6	14.0	26.0	14.6
16	613.4	13.3	296.2	144.1	94.9	85.3	38.6	15.4	10.9	21.2	11.3
24	425.3	19.2	205.6	98.6	69.2	57.5	26.4	11.3	7.8	18.9	7.7
32	357.2	22.9	169.0	73.9	53.7	49.4	21.5	9.4	6.7	16.5	6.0
48	271.0	30.2	121.9	52.9	47.5	35.4	16.8	7.7	5.1	16.1	4.2
64	241.7	33.9	105.5	43.4	41.5	31.8	13.9	7.5	4.8	16.0	3.3

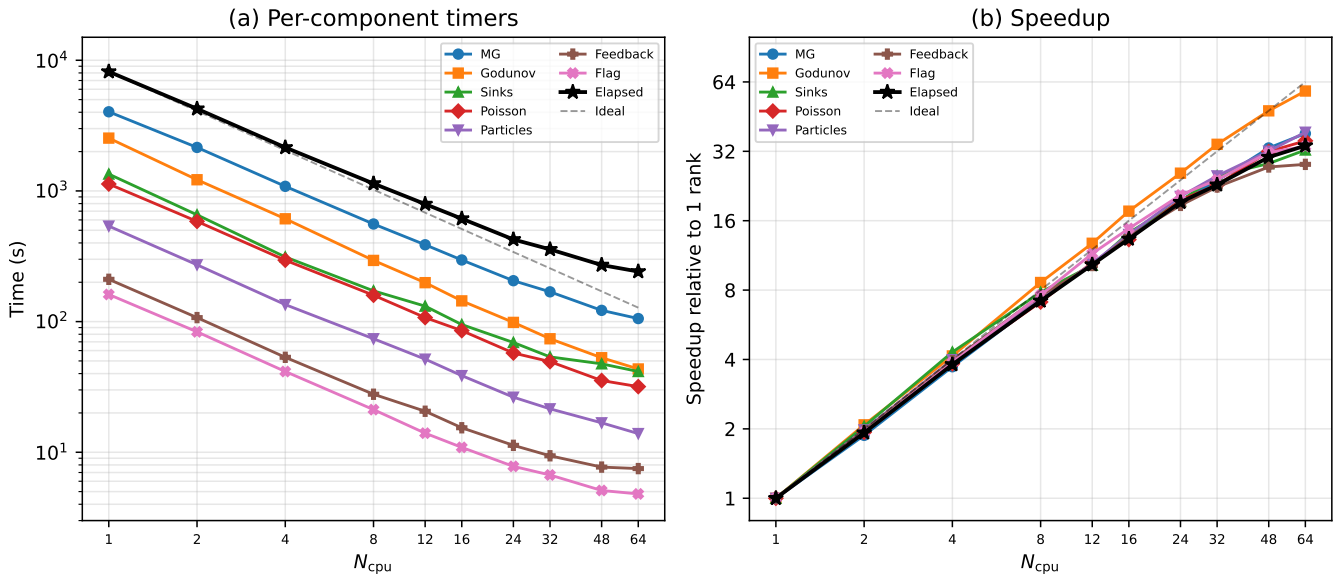


**Figure 3.** Strong scaling of CURAMSES on a dual-socket AMD EPYC 7543 node (64 cores) with a 135.7 M particle cosmological simulation including full physics. (a) Elapsed time and per-component wall-clock times versus  $N_{\text{cpu}}$ ; the dashed line shows ideal scaling from the single-rank baseline. (b) Speedup relative to 1 rank. Particle operations and the flag routine scale near-ideally, while the overall speedup reaches 33.9 $\times$  at 64 ranks (53% parallel efficiency).

946     (ii) **Morton key hash table.** A per-level open-addressing 964  
 947     hash table that replaces the 48-byte-per-grid `nbor` array 965  
 948     with  $\mathcal{O}(1)$  hash lookups, saving over 190 MB per rank at 966  
 949      $N_{\text{gridmax}} = 5$  M while simplifying the grid management code 967  
 950     (no neighbour-pointer maintenance during creation, deletion, 968  
 951     or migration). 969

952     (iii) **Memory optimizations.** On-demand allocation of 970  
 953     the Hilbert key, histogram, and defragmentation arrays re- 971  
 954     duces steady-state memory by over 1 GB per rank, enabling 972  
 955     larger problems or finer resolution within the same hardware 973  
 956     budget. 974

957     (iv) **Multigrid solver optimizations.** Precomputed 975  
 958     neighbour caches, merged red-black Gauss–Seidel sweeps (re- 976  
 959     ducing communication by 44 per cent per iteration), fused 977  
 960     residual-norm computation, and arithmetic optimizations 978  
 961     reduce the Poisson solver’s share of total runtime from 979  
 962     55 per cent to 39 per cent. 980

963     (v) **Feedback spatial binning.** A spatial hash binning 980

946     scheme reduces both SNII and AGN feedback computations 947  
 948     from  $\mathcal{O}(N_{\text{cells}} \times N_{\text{event}})$  to  $\mathcal{O}(N_{\text{cells}} \times 27 \bar{n}_{\text{event/bin}})$ , achieving 949  
 950     speedups of one to two orders of magnitude. 951

952     (vi) **Variable-ncpu restart.** Both HDF5 parallel I/O 953  
 954     and distributed binary I/O enable output/restart with ar- 955  
 956     bitrary rank counts, improving workflow flexibility for 957  
 957     production simulations on shared facilities. The binary path uses 958  
 959     round-robin file assignment and per-level MPI\_ALLTOALLV with 960  
 960     reusable exchange metadata. 961

961     (vii) **Hybrid CPU/GPU dispatch.** A dynamic dispatch 962  
 962     model in which OMP threads acquire GPU stream slots at 963  
 963     runtime, with fallback to CPU execution. Superbatch buffer- 964  
 964     ing amortises kernel launch latency, and an on-device scatter- 965  
 965     reduce kernel reduces PCIe transfer volume by 20 $\times$ . The Go- 966  
 966     dunov solver achieves a 16 per cent speedup on an RTX 5000 967  
 967     Ada GPU while producing bit-identical results. 968

968     All modifications preserve physical consistency, as verified 969

**Table 6.** Memory load balance for the strong-scaling test ( $54 M^{1016}$  grids, 135.7 M particles).  $M_{\min}$  and  $M_{\max}$  are the minimum and maximum per-rank resident memory after the final load-balance remap (step 243). The ratio  $M_{\max}/M_{\min}$  measures memory imbalance. The level-10 grid counts illustrate the per-rank work imbalance at the most populated refined level (19.5 M grids total).

$N_{\text{cpu}}$	$M_{\min}$ (Gb)	$M_{\max}$ (Gb)	$M_{\max}/M_{\min}$	Level-10 grids / rank		
				min	max	max/min
1	147.2	147.2	1.000	—	—	—
2	87.0	87.4	1.005	9 119 832	10 337 771 <sub>1021</sub>	—
4	50.1	50.5	1.008	4 545 882	5 209 834	—
8	28.0	28.6	1.021	2 199 595	2 675 391 <sub>1022</sub>	—
12	20.9	21.4	1.024	1 369 950	1 827 914 <sub>1023</sub>	—
16	16.7	17.1	1.024	1 021 171	1 375 737 <sub>1024</sub>	—
24	12.5	13.1	1.048	671 418	937 060 <sub>1025</sub>	—
32	10.7	11.1	1.037	521 392	710 999 <sub>1026</sub>	—
48	8.2	8.6	1.049	306 342	478 566 <sub>1027</sub>	—
64	8.2	8.6	1.049	224 830	362 435 <sub>1028</sub>	—

## DATA AVAILABILITY

The modified code is available at <https://github.com/kjhan0606/cuRAMSES-kjhan>. Test configurations and analysis scripts will be shared upon reasonable request to the author.

## REFERENCES

- Bryan G. L., et al., 2014, ApJS, 211, 19
- Dupois Y., et al., 2014, MNRAS, 444, 1453
- Dupois Y., et al., 2021, A&A, 651, A109
- Guillet T., Teyssier R., 2011, J. Comput. Phys., 230, 4756
- Hahn O., Abel T., 2011, MNRAS, 415, 2101
- Han S., et al., 2026, A&A, 705, A169
- Hopkins P. F., 2015, MNRAS, 450, 53
- Hopkins P. F., et al., 2018, MNRAS, 480, 800
- Knuth D. E., 1997, The Art of Computer Programming, Vol. 3: Sorting and Searching, 2nd edn. Addison-Wesley, Reading, MA
- Lee J., et al., 2021, ApJ, 908, 11
- Morton G. M., 1966, A Computer Oriented Geodetic Data Base and a New Technique in File Sequencing. IBM, Ottawa
- Nelson D., et al., 2019, Comput. Astrophys. Cosmol., 6, 2
- Pillepich A., et al., 2018, MNRAS, 473, 4077
- Schaye J., et al., 2015, MNRAS, 446, 521
- Springel V., 2005, MNRAS, 364, 1105
- Springel V., 2010, MNRAS, 401, 791
- Teyssier R., 2002, A&A, 385, 337
- Vogelsberger M., et al., 2014, MNRAS, 444, 1518
- Warren M. S., Salmon J. K., 1993, in Proc. Supercomputing '93. ACM, New York, p. 12

## APPENDIX A: K-SECTION TREE WALK PSEUDOCODE

Algorithm 2 gives the pseudocode for mapping a spatial position to its owning MPI rank by walking the  $k$ -section tree.

---

### Algorithm 2 CPU map computation via k-section tree walk

**Input:** Position  $\mathbf{x}$ , tree arrays

**Output:** CPU rank  $c$

```

1: node ← root
2:  $l \leftarrow 0$ 
3: while node is not a leaf do
4:    $l \leftarrow l + 1$ 
5:    $k \leftarrow k_l$ ; dir ← ksec_dir( $l$ )
6:   child ←  $k$ 
7:   for  $j = 1$  to  $k - 1$  do
8:     if  $x_{\text{dir}} \leq \text{ksec\_wall}(\text{node}, j)$  then
9:       child ←  $j$ ; break
10:    end if
11:   end for
12:   node ← ksec_next(node, child)
13: end while
14:  $c \leftarrow \text{ksec\_indx}(\text{node})$ 

```

---

## ACKNOWLEDGEMENTS

This work was supported by the Korea Institute for Advanced Study. Computational resources were provided by the KIAS Center for Advanced Computation. The author thanks Romain Teyssier for the public release of the RAMSES code and the RAMSES developer community for continued maintenance and improvements.

1048 **APPENDIX B: MORTON KEY ENCODING**  
 1049 **DETAILS**

1050 The Morton key interleaving for a single coordinate value  
 1051  $v$  with  $B = 21$  bits is computed by the following bit-  
 1052 manipulation loop:

---

**Algorithm 3** Morton key encoding of  $(i_x, i_y, i_z)$

---

**Input:** Integer coordinates  $(i_x, i_y, i_z)$

**Output:** 63-bit Morton key  $M$

```

1:  $M \leftarrow 0$ 
2: for  $b = 0$  to  $B - 1$  do
3:    $M \leftarrow M | (\text{bit}_b(i_x) \ll 3b)$ 
4:    $M \leftarrow M | (\text{bit}_b(i_y) \ll (3b + 1))$ 
5:    $M \leftarrow M | (\text{bit}_b(i_z) \ll (3b + 2))$ 
6: end for
```

---

1053 The neighbour key computation decodes, shifts the appro-  
 1054 priate coordinate, applies periodic wrapping, and re-encodes:

---

**Algorithm 4** Morton neighbour key in direction  $j$

---

**Input:** Morton key  $M$ , direction  $j$ , grid counts  $(n_x, n_y, n_z)$

**Output:** Neighbour Morton key  $M'$  (or  $-1$  if out of bounds)

```

1:  $(i_x, i_y, i_z) \leftarrow \text{DECODE}(M)$ 
2: Adjust  $i_d$  by  $\pm 1$  according to direction  $j$ 
3: Apply periodic wrapping:  $i_d \leftarrow i_d \bmod n_d$ 
4:  $M' \leftarrow \text{ENCODE}(i_x, i_y, i_z)$ 
```

---